SCIENCE CHINA
Chemistry

•ARTICLES•

November 2024 Vol.67 No.11: 3712–3718
https://doi.org/10.1007/s11426-024-2025-2

Integration of metal-organic layers with quantum dots for artificial photosynthesis

Hong Yuan, Min Zhang, Ji-Hua Deng*, Tong-Bu Lu & Di-Chang Zhong*

Institute for New Energy Materials and Low Carbon Technologies, School of Materials Science and Engineering, School of Chemistry and Chemical Engineering, Tianjin University of Technology, Tianjin 300384, China

Received March 2, 2024; accepted March 26, 2024; published online September 10, 2024

Metal-organic layers (MOLs), a type of new-emerging two-dimensional ultrathin metal-organic framework materials with large surface areas and highly exposed active sites, have shown promising applications in photocatalytic CO_2 reduction. However, due to a lack of photosensitivity and photooxidation capability, photosensitizers and sacrificial reductants are usually necessary for MOLs-based photocatalytic CO_2 reduction systems. In this article, by integration of MOLs and quantum dots (QDs), we constructed MOLs-based catalysts with multi-functions of photosensitivity, photoreduction and photooxidation, which thus can serve as photocatalysts for CO_2 reduction with H_2O as an electron donor. Specifically, by an electrostatic self-assembly approach, nickel(II)-based MOLs (Ni-MOLs) and $CsPbBr_3$ QDs have been assembled, constructing valid II-Scheme Ni-MOLs/$CsPbBr_3$ heterojunctions with close Ni-MOLs/$CsPbBr_3$ heterointerface. Such a close heterointerface shortens the charge transfer distance, thus effectively boosting the charge separation and transfer. As a result, upon illumination by visible light ($\lambda \geq 400$ nm, 100 mW cm^{-2}), the optimized photocatalyst shows high efficiency and stability in photochemical CO_2 reduction in the absence of any photosensitizers and sacrificial reductants. The CO yield reaches as high as 124 μmol g^{-1} in 4 h, over 6 times higher than that achieved by $CsPbBr_3$. Additionally, the selectivity reaches 100%. This work provides a new way to construct MOL-based catalysts for artificial photosynthesis.

metal-organic layers, artificial photosynthesis, CO_2 reduction, H_2O oxidation

Citation: Yuan H, Zhang M, Deng JH, Lu TB, Zhong DC. Integration of metal-organic layers with quantum dots for artificial photosynthesis. *Sci China Chem*, 2024, 67: 3712–3718, https://doi.org/10.1007/s11426-024-2025-2

1 Introduction

The excessive combustion of fossil fuels has led to a surge of carbon dioxide (CO_2) emission, which disrupts the equilibrium of the natural carbon cycle, resulting in global warming and severe climatic events [1–3]. For sustainable development, it is essential to reduce the CO_2 concentration in the atmosphere. Inspired by the natural photosynthesis of green plants, researcher has put forward the concept of artificial photosynthesis to photochemically convert CO_2 [4–7]. This is an ideal and effective approach for CO_2 conversion, through which not only the CO_2 concentration in the atmosphere can be reduced, but also the intermittent solar energy can be transformed into chemical energy to achieve the indirect storage of solar energy [8]. During the past several decades, photocatalytic CO_2 reduction technologies have undergone rapid development and obtained significant achievements [9–20]. However, the efficiency of artificial photosynthesis is still too low to meet the requirement of converting CO_2 excessively emitted. Therefore, albeit of great challenge, the development of high-performance artificial photosynthesis catalysts for CO_2 conversion is much desired.

Metal-organic frameworks (MOFs) have gained significant attention as a type of crystalline catalysts in CO_2

*Corresponding authors (email: djhycu_2006@aliyun.com; zhong_dichang@hotmail.com)

reduction [21–24]. The definite catalytic centers and precise coordination environments around the catalytic centers benefit for revealing the performance-structure relationship of catalysts in CO_2 reduction. Metal-organic layers (MOLs) possess two-dimensional ultrathin layer structures and could be regarded as the subclass of MOFs. Their structural features, including large surface areas and highly exposed active sites, have enabled MOLs to be more promising in photocatalytic CO_2 reduction [25–29]. However, the majority of MOLs exhibit limited response to visible light and lack the ability to oxidize water, necessitating the incorporation of precious metal photosensitizers and sacrificial reagents to construct effective catalytic systems for driving photocatalytic CO_2 reduction [30,31].

Halide perovskites are a type of important light-harvesting materials that possess superiority of cost-effective preparation, visible-light response, substantial extinction coefficient, and extended photogenerated carrier lifetime, thus demonstrating huge potential in photocatalysis [10,32–34]. Particularly, the halide perovskite materials, such as $CsPbBr_3$ quantum dots (QDs), have photocatalytic H_2O oxidation capability, which enables them to attract more attention in artificial photosynthesis [35,36].

Our group has been devoting efforts to developing MOLs-based catalysts for energy conversion and storage during the past several years [26]. Very recently, we used MOLs as a platform to demonstrate that the photocatalytic activity of MOFs for CO_2 photoreduction is closely related to their crystal facets [30]. We found that Ni-MOLs with richly exposed (100) crystal facets (Ni-MOL-100) show superior photocatalytic activity over those with richly exposed (010) crystal facets (Ni-MOL-010). However, in this case, noble-metal photosensitizer of $Ru(phen)_3(PF_6)_2$ and sacrificial agent of triethanolamine (TEOA) are necessary to drive the photocatalytic CO_2 reduction reaction. To circumvent the issue and achieve artificial photosynthesis ($CO_2 + H_2O \rightarrow$ organic compounds + O_2), endowing the Ni-MOLs with light-harvesting and water-oxidation capacity is indispensable. With the above points in mind, we tried to build efficient heterojunction materials between MOLs and halide perovskite QDs to achieve artificial photosynthesis. In this paper, we, for the first time, constructed a valid II-Scheme heterojunction between nickel(II)-based MOLs (Ni-MOLs) and $CsPbBr_3$ QDs by an electrostatic self-assembly approach. The resulting Ni-MOLs/$CsPbBr_3$ heterojunction not only integrates multi-functions of light-harvesting, photoreduction and photooxidation, but also has a close heterointerface, effectively boosting the charge separation and transfer. As a result, upon illumination by visible light ($\lambda \geq$ 400 nm, 100 mW cm^{-2}), the optimized Ni-MOLs/$CsPbBr_3$ heterojunction photocatalysts show high activity in photochemical CO_2 reduction in the absence of any photosensitizers and sacrificial reductants. The CO yield reaches as high as 124 μmol g^{-1}, over 6 times higher than that achieved by $CsPbBr_3$ QDs. Additionally, the selectivity reaches 100%. The excellent catalytic performance of the heterojunction photocatalyst can be ascribed to the combination of both superiorities of Ni-MOLs and $CsPbBr_3$ QDs, which provides a new way for constructing efficient artificial photosynthesis catalysts based on MOLs.

2 Experimental

2.1 Synthesis of Ni-MOLs/$CsPbBr_3$

Ni-MOLs exposing (100) and (010) crystal facets (designated as Ni-MOL-100 and Ni-MOL-010, respectively) were first synthesized by the reaction of nickel nitrate, terephthalic acid and sodium hydroxide in DMF and H_2O at 120 °C at different concentrations of NaOH (Supporting Information online) [30]. $CsPbBr_3$ QDs were then synthesized using the conventional hot injection method (Figure S1, Supporting Information online). Finally, the integration of Ni-MOLs with $CsPbBr_3$ was performed via electrostatic interaction (Scheme 1). Specifically, as the zeta potentials of Ni-MOLs dispersed in acetonitrile and $CsPbBr_3$ QDs dispersed in *n*-hexane were measured to be −178.7 and +24.2 mV, respectively (Figure S2), the opposite surface charges drive the combination of Ni-MOLs and $CsPbBr_3$, to construct Ni-MOLs/$CsPbBr_3$ heterojunctions with tightly contact heterointerface [34]. Five types of Ni-MOL-100/$CsPbBr_3$ composites with different weight ratios of Ni-MOL-100 to $CsPbBr_3$ QDs (2/1, 1/1, 1/3, 1/5 and 1/7) were obtained. Furthermore, the metal contents of Ni, Cs and Pb in Ni-MOL-100/$CsPbBr_3$ in these composites were determined by inductively coupled plasma-mass spectroscopy (ICP-MS, Table S1, Supporting Information online).

2.2 Photocatalytic CO_2 reduction experiments

The photocatalytic CO_2 reduction reactions were performed using a gas-solid apparatus with a 17 mL sealed quartz bottle at room temperature. Specifically, 2.0 mg of photocatalyst and 30 μL deionized H_2O were added into the reaction system. Before the photocatalytic reaction, the reaction apparatus was degassed and refilled with CO_2 and H_2O vapor for

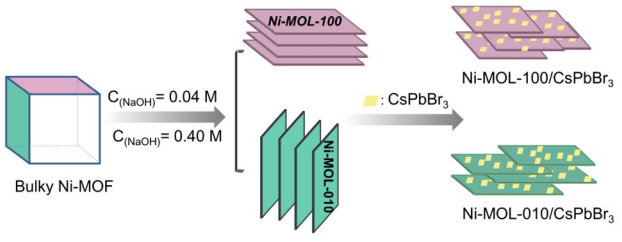

Scheme 1 Schematic diagram showing the preparation of Ni-MOLs/$CsPbBr_3$ heterojunctions (color online).

25 min to remove air. A 300 W Xe lamp irradiated the reaction system ($\lambda \geq 400$ nm, 100 mW cm^{-2}). The gaseous products possibly generated were detected by gas chromatography.

3 Results and discussion

The results of powder X-ray diffraction (PXRD) measurements show that the PXRD patterns of Ni-MOLs exposing (100) and (010) crystal facets are consistent with those reported [30], with the characteristic peaks observed at 9.3°, 11.9° and 23.8° assigned to the (100), (010) and (020) crystallographic facets of Ni-MOLs, respectively. The different intensities of diffraction peaks corresponding to (100) and (010) crystal facets illustrate that Ni-MOL-100 and Ni-MOL-010 have been successfully synthesized (Figure 1a). Transmission electron microscopy (TEM) measurements show the ultrathin layer morphology of the Ni-MOLs, which are also consistent with the reported [30], also evidencing the successful synthesis of Ni-MOL-100 and Ni-MOL-010 (Figure 2a–c). These ultrathin nanosheets may favor the mutual Coulomb electrostatic assembly with opposite charge materials. Moreover, these ultrathin nanosheets with large surface area can provide abundant catalytic active sites and greatly shorten the transport distance of photogenerated charge carriers, benefiting to boost photocatalysis [37,38].

The PXRD patterns of the synthesized $CsPbBr_3$ QDs show diffraction peaks at 14.9°, 21.1°, 26.3°, 30.4°, 37.4° and 43.4°, which can be assigned to (100), (110), (111), (200), (211) and (202) crystal facets of $CsPbBr_3$ QDs, respectively (Figure 1b), consistent with the XRD standard card for $CsPbBr_3$ QDs (JCPDS: 00-054-0572) [39]. In addition, the TEM images show that the synthesized $CsPbBr_3$ QDs assume rectangular morphology, with the particle size of about 8 nm (Figure 2d and Figure S3) and the lattice spacing of 0.58 nm, which can be assigned to the (100) crystal facet (Figure S4). These results also illustrate that $CsPbBr_3$ QDs, as reported, have been successfully prepared [40]. The PXRD patterns of the composites exhibit diffraction peaks of both Ni-MOLs and $CsPbBr_3$ QDs (Figure 1c, d), which indicates the successful integration of Ni-MOLs and $CsPbBr_3$ QDs. The observation also illustrates that each component in the composite keeps the same crystal phase as the single Ni-MOLs or $CsPbBr_3$ QDs. TEM images clearly show that rectangular, square pieces of $CsPbBr_3$ QDs were uniformly mounted onto the initially smooth Ni-MOLs nanosheets (Figure 2e, f). This visually confirms the successful synthesis of Ni-MOLs/$CsPbBr_3$ composites.

The optical properties of Ni-MOL-100/$CsPbBr_3$ composites and the corresponding single components were investigated by ultraviolet-visible (UV-Vis) absorption spectra and Mot-shottky tests. As depicted in Figure 3a, compared

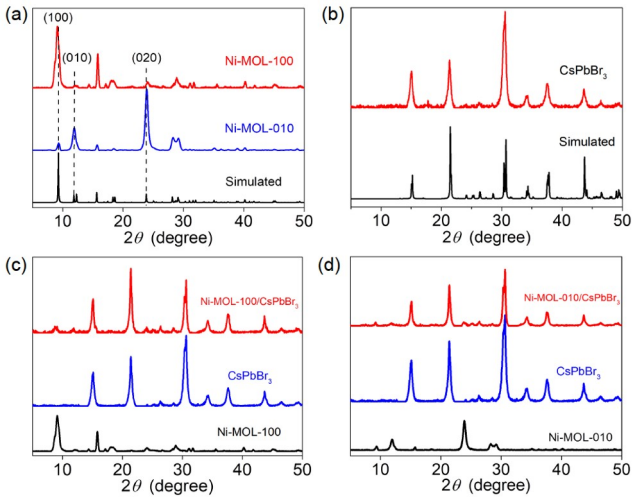

Figure 1 PXRD patterns of as-prepared (a) Ni-MOLs, (b) $CsPbBr_3$ QDs, and (c) Ni-MOL-100/$CsPbBr_3$ and (d) Ni-MOL-010/$CsPbBr_3$ (color online).

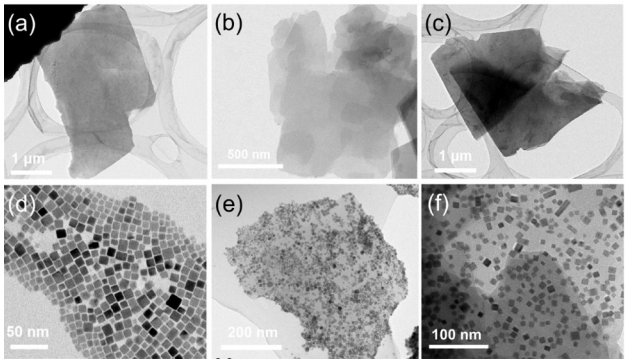

Figure 2 TEM images of (a, b) Ni-MOL-100, (c) Ni-MOL-010, (d) $CsPbBr_3$ and (e, f) Ni-MOL-100/$CsPbBr_3$.

with the single Ni-MOL-100, the incorporation of $CsPbBr_3$ QDs into Ni-MOL-100 expands the range of light absorption in the visible light region and enhances the intensity of the light absorption. In contrast to $CsPbBr_3$, the UV-Vis absorption spectrum of Ni-MOL-100/$CsPbBr_3$ shows a slight redshift of the absorption edge. This observation indicates the strong interfacial interaction between Ni-MOL-100 and $CsPbBr_3$ in the 2D/0D heterostructure [41].

Based on the above UV-Vis diffuse reflectance spectra, the band gaps of Ni-MOL-100 and $CsPbBr_3$ QDs were determined by Tauc plots method (Figure 3b), which results in the values of 3.17 and 2.11 eV for Ni-MOL-100 and $CsPbBr_3$ QDs, respectively. By Mott-Schottky plots, it can be inferred that the lowest unoccupied molecular orbital potential (LUMO) of Ni-MOLs and the conduction band (CB) potential of $CsPbBr_3$ QDs are −0.77 and −1.02 V *vs.* NHE, respectively (Figure 3c, d). Consequently, the highest occupied molecular orbital potential (HOMO) of Ni-MOL-100 and the valence band (VB) potential of $CsPbBr_3$ QDs can be calculated to be +2.40 and +1.09 V *vs.* NHE, respectively

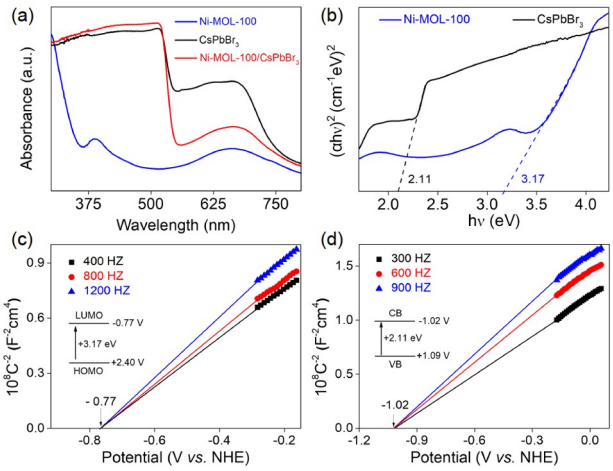

Figure 3 (a) UV/Vis absorption spectra of Ni-MOL-100, $CsPbBr_3$ and Ni-MOL-100/$CsPbBr_3$; (b) Tauc plots of Ni-MOL-100 and $CsPbBr_3$; (c, d) Mott-Schottky plots of Ni-MOL-100 and $CsPbBr_3$ (color online).

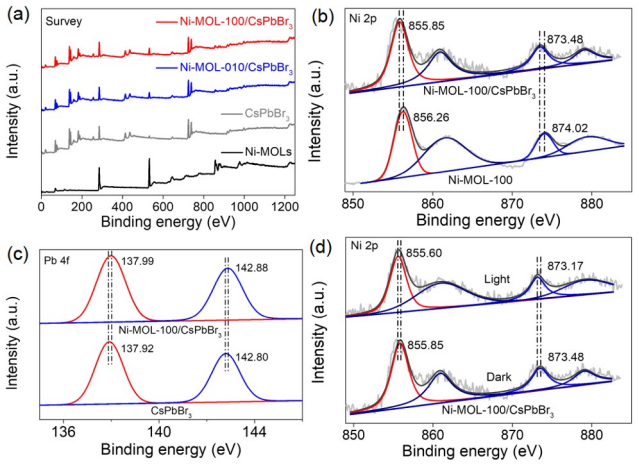

Figure 4 High-resolution XPS spectra of as-prepared samples. (a) Full spectra analysis; (b) Ni 2p XPS spectra of Ni-MOL-100/$CsPbBr_3$ and Ni-MOL-100; (c) Pb 4f XPS spectra of Ni-MOL-100/$CsPbBr_3$ and $CsPbBr_3$; (d) Ni 2p XPS spectra of Ni-MOL-100/$CsPbBr_3$ under dark or light-irradiation conditions (color online).

(Figure 3c, d). On the basis of these results, the energy level structure of Ni-MOL-100 and band structure of $CsPbBr_3$ QDs could be determined, as inset in Figure 3c, d.

X-ray photoelectron spectroscopy (XPS) measurements were carried out to investigate the surface chemical state and elemental composition of the synthesized samples. As presented in Figure 4a, the XPS survey spectrum confirms the existence of Ni, Cs, Pb, Br, O, N and C in the Ni-MOLs/$CsPbBr_3$. In contrast to pure $CsPbBr_3$, two new peaks at about 856 and 874 eV assignable to Ni $2p_{3/2}$ and Ni $2p_{1/2}$ can be clearly observed in the high-resolution XPS spectrum of Ni-MOLs/$CsPbBr_3$ (Figure 4a, b). Furthermore, there are perceptible shifts of binding energies for Ni 2p (Figure 4b and Figure S5), Pb 4f (Figure 4c and Figure S6), Cs 3d (Figures S7, S8), and Br 3d (Figures S9, S10) in Ni-MOLs/$CsPbBr_3$ in comparison with those in individual Ni-MOLs and $CsPbBr_3$, suggesting strong electronic coupling between Ni-MOLs and $CsPbBr_3$ in Ni-MOLs/$CsPbBr_3$ heterojunction [30,42].

The charge transfer route was further revealed by XPS spectra measured under light irradiation. As shown in Figure 4d, the binding energies of Ni 2p of Ni-MOL-100/$CsPbBr_3$ under light irradiation shift negatively by 0.25 eV with reference to those measured in dark conditions. Conversely, the binding energies of Cs 3d (Figure S11) and Pb 4f (Figure S12) of Ni-MOL-100/$CsPbBr_3$ shift positively by ~0.2 eV. Similar phenomena are observed for Ni 2p, Cs 3d and Pb 4f of Ni-MOL-010/$CsPbBr_3$ (Figures S13–S15). These observations unequivocally prove that the photoexcited electrons in the CB of $CsPbBr_3$ transfer to the LUMO of Ni-MOLs under light irradiation, following an II-scheme pathway [43,44]. Obviously, the enhanced electron density on Ni-MOLs will facilitate the CO_2 reduction.

Steady-state photoluminescence (PL) spectra were further measured to investigate the dynamics of photogenerated carriers in Ni-MOLs/$CsPbBr_3$. As depicted in Figure 5a, the pristine $CsPbBr_3$ demonstrates a robust PL emission with a characteristic peak centered at 517 nm. In contrast, Ni-MOL-010/$CsPbBr_3$ and Ni-MOL-100/$CsPbBr_3$ show markedly lower PL intensity, implying that the presence of Ni-MOLs efficiently retards the electron-hole recombination in $CsPbBr_3$. Furthermore, Ni-MOL-100/$CsPbBr_3$ exhibits more pronounced quenching of PL compared to Ni-MOL-010/$CsPbBr_3$, highlighting its distinct advantage in facilitating interfacial charge transfer over Ni-MOL-010/$CsPbBr_3$. To gain a deeper insight into the charge transfer dynamics, the time-resolved photoluminescence (TRPL) spectra of $CsPbBr_3$, Ni-MOL-010/$CsPbBr_3$ and Ni-MOL-100/$CsPbBr_3$ were recorded at detection wavelength (EW) of 520 nm (Figure 5b), corresponding to the maximum fluorescence emissions of $CsPbBr_3$. The fitted decay curves disclose the lifetime (τ) and percentage (Rel.%) of charge carriers (Figure S16 and Table S2). The results show that the average emission lifetime significantly decreases from 23.50, 19.94, to 12.31 ns for $CsPbBr_3$, Ni-MOL-010/$CsPbBr_3$, and Ni-MOL-100/$CsPbBr_3$, respectively. Moreover, the contribution of τ_1, the fast decay component related to charge transfer, enhances obviously the contrary to the trend of τ_3, the slow decay component related to radiative recombination [32,45,46]. These results reveal that the integration of Ni-MOLs and $CsPbBr_3$ provides extra charge transfer channels, thus efficiently inhibiting the electron-hole recombination of $CsPbBr_3$.

The efficient interfacial charge transfer of Ni-MOLs/$CsPbBr_3$ was further corroborated by photoelectrochemical analysis. As presented in Figure 5c, Ni-MOL-100/$CsPbBr_3$ exhibits a significantly larger photocurrent density with re-

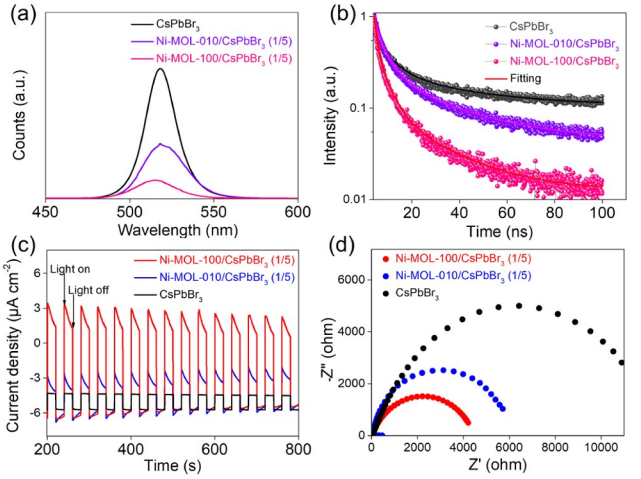

Figure 5 (a) PL spectra of $CsPbBr_3$, Ni-MOL-010/$CsPbBr_3$ and Ni-MOL-100/$CsPbBr_3$. (b) TRPL spectra of $CsPbBr_3$, Ni-MOL-010/$CsPbBr_3$ and Ni-MOL-100/$CsPbBr_3$ at detection wavelength of 520 nm. (c) *I-t* curves of $CsPbBr_3$, Ni-MOL-010/$CsPbBr_3$ and Ni-MOL-100/$CsPbBr_3$ plotted at a bias potential of −0.4 V (*vs.* Ag/AgCl) under light illumination (100 mW cm^{-2}). (d) EIS Nyquist plots of $CsPbBr_3$, Ni-MOL-010/$CsPbBr_3$ and Ni-MOL-100/$CsPbBr_3$ measured under dark (color online).

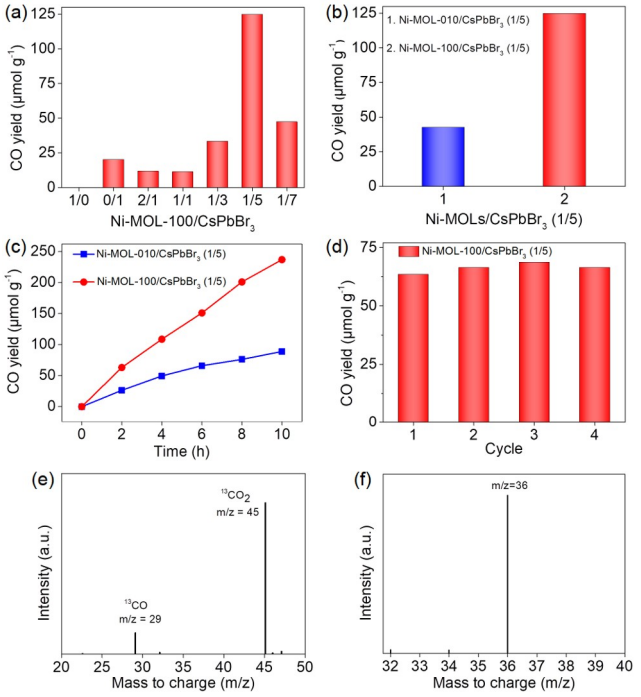

Figure 6 (a) CO yield of Ni-MOL-100/$CsPbBr_3$ with different mass ratios of Ni-MOL-100 and $CsPbBr_3$ for 4 h. (b) CO yield of Ni-MOL-010/$CsPbBr_3$ (1/5) and Ni-MOL-100/$CsPbBr_3$ (1/5) for 4 h. (c) Time-dependent CO generated from photocatalytic CO_2 reduction by Ni-MOL-100/$CsPbBr_3$ (1/5) and Ni-MOL-010/$CsPbBr_3$ (1/5). (d) Durable tests of Ni-MOL-100/$CsPbBr_3$ for photocatalytic CO_2 reduction (Each cycle was tested for 2h). (e) Mass spectra (MS) analyses for product generated from the photocatalytic $^{13}CO_2$ reduction in the presence of H_2O by Ni-MOL-100/$CsPbBr_3$. (f) Mass spectra (MS) analyses for product generated from the photocatalytic CO_2 reduction in the presence of $H_2{}^{18}O$ by Ni-MOL-100/$CsPbBr_3$ (color online).

spect to Ni-MOL-010/$CsPbBr_3$ and $CsPbBr_3$. In addition, the electrochemical impedance spectra (EIS) show Ni-MOL-100/$CsPbBr_3$ exhibits a smaller semicircle compared with Ni-MOL-010/$CsPbBr_3$ and pure $CsPbBr_3$ (Figure 5d), suggesting a lower charge-transfer resistance. All these results elucidate the enhanced photoactivity after the composite of Ni-MOLs with $CsPbBr_3$ [47].

Photocatalytic CO_2 reduction experiments of Ni-MOLs/$CsPbBr_3$ were conducted in a gas-solid reactor filled with CO_2 and H_2O vapor under visible-light irradiation ($\lambda \geq$ 400 nm, 100 mW cm^{-2}) and without addition of any noble-metal photosensitizer and electron sacrificial reagent. The photocatalytic activity of individual Ni-MOLs and $CsPbBr_3$ was also assessed under the same condition. The chromatographic analyses identified that the CO was generated as the only product for Ni-MOLs/$CsPbBr_3$, and no byproduct of H_2 was detected. As shown in Figure 6a, without $CsPbBr_3$, no CO was generated in photocatalytic CO_2 reduction by Ni-MOLs. Increasing the mass ratio of $CsPbBr_3$, the photocatalytic performance of Ni-MOLs-100/$CsPbBr_3$ increases first and then decreases subsequently, and the sample with the mass ratio of 1/5 shows the optimal performance. It can be reasoned that the initially increased amount of $CsPbBr_3$ could help to improve the light absorption of the composite, but excessive $CsPbBr_3$ would decrease the effective heterointerface area and lead to the decrease of catalytic performance. With the mass ratio of 1/5, the CO yield of Ni-MOLs-100/$CsPbBr_3$ reaches as high as 124 μmol g^{-1} upon illumination for 4 h, with the selectivity of 100%. This value is much higher than that of the reported MOF/MOL-based artificial photosynthesis catalysts under the same conditions, in spite of being slightly lower than those under strong light sources (Table S3). The greatly enhanced catalytic performance of Ni-MOLs-100/$CsPbBr_3$ can be attributed to the effective 2D/0D II-scheme heterojunction between Ni-MOLs-100 and $CsPbBr_3$, as well as the close interface between them analyzed above, which can greatly accelerate the separation and transfer of photogenerated charge, thus significantly boosting the photocatalytic activity for CO_2 reduction [37,38].

It is worth mentioning that Ni-MOL-010/$CsPbBr_3$ also shows much better photocatalytic activity for CO_2 reduction than individual Ni-MOL-010 and $CsPbBr_3$. However, it exhibits lower activity than Ni-MOL-100/$CsPbBr_3$ (Figure 6b, c). This can be ascribed to the structure difference between (100) and (010) crystal facets in Ni-MOF. The Ni(II) in the (100) crystal facet could generate a synergistic catalysis effect for CO_2 reduction, while those in the (010) crystal facet are constrained by spatial configuration; thus, no synergistic catalysis effect generated, which is consistent with our previously results [30].

Besides high activity, Ni-MOL-100/$CsPbBr_3$ also exhibits excellent stability in photocatalytic CO_2 reduction. As shown

in Figure 6d, during four runs of photocatalytic CO_2 reduction by Ni-MOL-100/$CsPbBr_3$, the CO yield is nearly unchanged, indicating the good stability of Ni-MOL-100/$CsPbBr_3$ in the gas-solid catalytic system. After the reaction, the catalyst was tested by PXRD. The results show that the PXRD patterns of Ni-MOLs/$CsPbBr_3$ after catalytic reaction are almost the same as those freshly prepared (Figure S17), further illustrating the robustness of the composite photocatalysts. We also tested the photocatalytic CO_2 reduction experiment by Ni-MOL-100/$CsPbBr_3$ and $CsPbBr_3$ over a long time (33 and 12 h, respectively). As shown in Figure S18, the amount of CO generated is almost linearly with the increased time. However, the $CsPbBr_3$ is deactivated after 10 h. These results indicate that the integrated Ni-MOL-100 could protect the $CsPbBr_3$ and confirms that Ni-MOL-100/$CsPbBr_3$ really possesses excellent catalytic stability during the process of CO_2 photoreduction.

A series of control experiments were carried out to investigate the photocatalytic CO_2 reduction over Ni-MOL-100/$CsPbBr_3$. It is found that very limited CO is detected when N_2 is used instead of CO_2 (Figure S19), which may be a result of the photooxidation of organic species residues on the surface of $CsPbBr_3$ [48]. At the same time, no products are detected in the absence of Ni-MOL-100/$CsPbBr_3$ or light irradiation, indicating that the CO_2 reduction reaction is triggered by light illumination. It should be noted that without water vapor, CO production is also negligible, indicating that the electron source of CO_2 photoreduction comes from the oxidation of water. This conclusion was further confirmed by isotope-labeled experiments. As shown in Figure 6e, f, when $^{13}CO_2$ and $H_2{}^{18}O$ are used instead of $^{12}CO_2$ and $H_2{}^{16}O$, the mass spectrometry shows peaks at m/z = 29 and 36, which corresponds to the signals of ^{13}CO and $^{18}O_2$, respectively. This result solidly proves that CO and O_2 are derived from CO_2 photoreduction and H_2O photooxidation.

In situ Fourier transform infrared (FTIR) measurements were carried out to monitor the reaction intermediates in the photocatalytic CO_2 reduction (Figure 7a), in which two absorption peaks at 1,636 and 2,077 cm^{-1} corresponding to *COOH and *CO intermediates can be clearly observed. It is well-known that both *COOH and *CO are crucial intermediates during the process of CO_2 reduction to CO. The FTIR result well monitors the process of photocatalytic CO_2 reduction to CO by Ni-MOL-100/$CsPbBr_3$. The gradual increase of the *COOH concentration also suggests the rate-limiting step for CO_2 reduction to CO by Ni-MOLs/$CsPbBr_3$ is the formation of *CO (*COOH + H^+ + e^- → *CO + H_2O) [19,49,50].

Based on the above-mentioned analysis of *in situ* XPS, PL, TRPL, photocurrent response and electrochemical impedance spectroscopy (EIS), we propose a plausible electron transfer mechanism and corresponding photocatalytic pathway for CO_2 reduction by Ni-MOLs/$CsPbBr_3$. The Ni-MOLs and $CsPbBr_3$ QDs in the Ni-MOLs/$CsPbBr_3$ composites can be excited by visible light, leading to the generation of electrons, as illustrated in Figure 7b. The CB potential of $CsPbBr_3$ QDs (–1.02 eV *vs*. NHE, Figure 3d, inset) is more negative than the LUMO potential of Ni-MOLs (–0.77 eV *vs*. NHE, Figure 3c, inset). The photoexcited electrons in the CB of $CsPbBr_3$ can directly transfer to the LUMO of Ni-MOLs, where the Ni(II) serves as the catalytic center for CO_2 reduction. On the other hand, the photogenerated holes in the HOMO of Ni-MOLs can directly transfer to the VB of $CsPbBr_3$, which serves as the catalytic center for H_2O oxidation. The spatial separation of photoinduced electrons and holes effectively suppresses their recombination and prolongs the lifetime of photoinduced carriers, which endows the Ni-MOLs/$CsPbBr_3$ with high performance in photocatalytic CO_2 reduction.

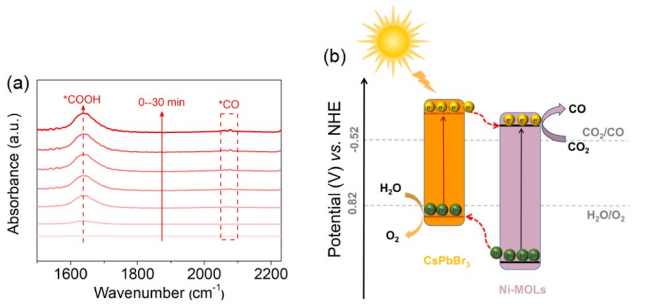

Figure 7 (a) *In situ* FTIR spectra of Ni-MOL-100/$CsPbBr_3$ during the photocatalytic CO_2 reduction. (b) Schematic illustration of the possible mechanism of photocatalytic CO_2 reduction by Ni-MOLs/$CsPbBr_3$ (color online).

4 Conclusions

In summary, by integration of Ni-MOLs and $CsPbBr_3$, a type of MOLs-based photocatalysts possessing multi-functions of photosensitivity, photoreduction and photooxidation have been fabricated. The multi-functions enable these catalysts to be active in visible-light-driven CO_2 reduction with H_2O as an electron donor. The optimized photocatalyst shows much higher efficiency than pristine Ni-MOLs and $CsPbBr_3$ QDs under the same conditions, with the CO yield reaching as high as 124 μmol g^{-1}, and the selectivity of 100%. The remarkable enhancement in photocatalytic activity can be attributed to the efficient charge separation and transfer occurring at the interface between Ni-MOLs and $CsPbBr_3$ QDs. This work provides a new way to construct MOL-based catalysts for artificial photosynthesis.

Acknowledgements This work was supported by the National Natural Science Foundation of China (22071182, 22271218, 21931007) and the National Key R&D Program of China (2022YFA1502902).

Conflict of interest The authors declare no conflict of interest.

Supporting information The supporting information is available online at http://chem.scichina.com and http://link.springer.com/journal/11426. The supporting materials are published as submitted, without typesetting or editing. The responsibility for scientific accuracy and content remains entirely with the authors.

1 Shakun JD, Clark PU, He F, Marcott SA, Mix AC, Liu Z, Otto-Bliesner B, Schmittner A, Bard E. *Nature*, 2012, 484: 49–54
2 Gao W, Liang S, Wang R, Jiang Q, Zhang Y, Zheng Q, Xie B, Toe CY, Zhu X, Wang J, Huang L, Gao Y, Wang Z, Jo C, Wang Q, Wang L, Liu Y, Louis B, Scott J, Roger AC, Amal R, He H, Park SE. *Chem Soc Rev*, 2020, 49: 8584–8686
3 Men YL, Liu P, Peng X, Pan YX. *Sci China Chem*, 2020, 63: 1416–1427
4 Mo G, Wang Q, Lu W, Wang C, Li P. *Chin J Chem*, 2022, 41: 335–354
5 Lu M, Zhang M, Liu J, Chen Y, Liao J, Yang M, Cai Y, Li S, Lan Y. *Angew Chem Int Ed*, 2022, 61: e202200003
6 Yang Y, Zhang HY, Wang Y, Shao LH, Fang L, Dong H, Lu M, Dong LZ, Lan YQ, Zhang FM. *Adv Mater*, 2023, 35: 2340170
7 Zhang B, Sun L. *Chem Soc Rev*, 2019, 48: 2216–2264
8 Montoya JH, Seitz LC, Chakthranont P, Vojvodic A, Jaramillo TF, Nørskov JK. *Nat Mater*, 2016, 16: 70–81
9 Zhang JH, Gong YN, Wang HJ, Wang YC, Yang W, Mei JH, Zhong DC, Lu TB. *Proc Natl Acad Sci USA*, 2022, 119: e2118278119
10 Wu L, Mu Y, Guo X, Zhang W, Zhang Z, Zhang M, Lu T. *Angew Chem Int Ed*, 2019, 58: 9491–9495
11 Li X, Sun Y, Xu J, Shao Y, Wu J, Xu X, Pan Y, Ju H, Zhu J, Xie Y. *Nat Energy*, 2019, 4: 690–699
12 Jiang Z, Xu X, Ma Y, Cho HS, Ding D, Wang C, Wu J, Oleynikov P, Jia M, Cheng J, Zhou Y, Terasaki O, Peng T, Zan L, Deng H. *Nature*, 2020, 586: 549–554
13 Yang W, Xu M, Tao K, Zhang J, Zhong D, Lu T. *Small*, 2022, 18: 2200332
14 Zhang C, Xie C, Gao Y, Tao X, Ding C, Fan F, Jiang H. *Angew Chem Int Ed*, 2022, 61: e202204108
15 Gong Y, Mei J, Shi W, Liu J, Zhong D, Lu T. *Angew Chem Int Ed*, 2024, 63: e202318735
16 Wu Y, Wu M, Zhu J, Zhang X, Li J, Zheng K, Hu J, Liu C, Pan Y, Zhu J, Sun Y, Xie Y. *Sci China Chem*, 2023, 66: 1997–2003
17 Yang W, Lin X, Shi WJ, Zhang JH, Wang YC, Deng JH, Zhong DC, Lu TB. *J Mater Chem A*, 2023, 11: 2225–2232
18 Ren F, Luo W, Zou Z. *Sci China Chem*, 2019, 62: 1553–1554
19 Ming MT, Wang YC, Tao WX, Shi WJ, Zhong DC, Lu TB. *Green Chem*, 2023, 25: 6207–6211
20 Zhang J, Wang Y, Wang H, Zhong D, Lu T. *Chin Chem Lett*, 2022, 33: 2065–2068
21 Sun K, Qian Y, Jiang H. *Angew Chem Int Ed*, 2023, 62: e202217565
22 Zuo Q, Cui R, Wang L, Wang Y, Yu C, Wu L, Mai Y, Zhou Y. *Sci China Chem*, 2023, 66: 570–577
23 Zeng JY, Wang XS, Xie BR, Li QR, Zhang XZ. *J Am Chem Soc*, 2022, 144: 1218–1231
24 Zuo JL. *Sci China Chem*, 2019, 62: 1263–1264
25 Deng JH, Wen YQ, Willman J, Liu WJ, Gong YN, Zhong DC, Lu TB, Zhou HC. *Inorg Chem*, 2019, 58: 11020–11027
26 Wang H, Zhang C, Dong B, Zhong D, Lu T. *Sci China Mater*, 2023, 66: 839–858
27 Zhang JH, Yang W, Zhang M, Wang HJ, Si R, Zhong DC, Lu TB. *Nano Energy*, 2021, 80: 105542–105550
28 Wang Y, Zhang Z, Li J, Yuan Y, Yang J, Xu W, An P, Xi S, Guo J, Liu B, Li J. *Angew Chem Int Ed*, 2022, 61: e202211031
29 Li A, Zhang Y, Sun Z, Niu Z, Lan G. *Sci China Chem*, 2023, 66: 3372–3382
30 Yang W, Wang H, Liu R, Wang J, Zhang C, Li C, Zhong D, Lu T. *Angew Chem Int Ed*, 2020, 60: 409–414
31 Wang W, Zhang Y, Wu A, He L. *Chem Eur J*, 2022, 28: e202201767
32 Xu F, Meng K, Cheng B, Wang S, Xu J, Yu J. *Nat Commun*, 2020, 11: 4613–4621
33 Qiao GY, Guan D, Yuan S, Rao H, Chen X, Wang JA, Qin JS, Xu JJ, Yu J. *J Am Chem Soc*, 2021, 143: 14253–14260
34 Wang Z, Lin Q, Wenger B, Christoforo MG, Lin YH, Klug MT, Johnston MB, Herz LM, Snaith HJ. *Nat Energy*, 2018, 3: 855–861
35 Ou M, Tu W, Yin S, Xing W, Wu S, Wang H, Wan S, Zhong Q, Xu R. *Angew Chem Int Ed*, 2018, 57: 13570–13574
36 Tan Y, Zhao H, Xu Q. *Sci China Mater*, 2024, 67: 1150–1159
37 Low J, Yu J, Jaroniec M, Wageh S, Al-Ghamdi AA. *Adv Mater*, 2017, 29: 1601694
38 Su J, Li G, Li X, Chen J. *Adv Sci*, 2019, 6: 1801702
39 Mu Y, Zhang W, Dong G, Su K, Zhang M, Lu T. *Small*, 2020, 16: 2002140
40 Su K, Yuan S, Wu L, Liu Z, Zhang M, Lu T. *Small*, 2023, 19: 2301192
41 Zhu M, Kim S, Mao L, Fujitsuka M, Zhang J, Wang X, Majima T. *J Am Chem Soc*, 2017, 139: 13234–13242
42 Jiang Y, Liao JF, Chen HY, Zhang HH, Li JY, Wang XD, Kuang DB. *Chem*, 2020, 6: 766–780
43 Wang H, Niu R, Liu J, Guo S, Yang Y, Liu Z, Li J. *Nano Res*, 2022, 15: 6987–6998
44 Niu Y, Jiang J, Fang X, Zhang F, Wang Y. *Solid State Sci*, 2024, 147: 107407
45 Zhang YX, Wang HY, Zhang ZY, Zhang Y, Sun C, Yue YY, Wang L, Chen QD, Sun HB. *Phys Chem Chem Phys*, 2017, 19: 1920–1926
46 Wu K, Liang G, Shang Q, Ren Y, Kong D, Lian T. *J Am Chem Soc*, 2015, 137: 12792–12795
47 Fu J, Jiang K, Qiu X, Yu J, Liu M. *Mater Today*, 2020, 32: 222–243
48 Xu Y, Zhang W, Su K, Feng Y, Mu Y, Zhang M, Lu T. *Chem Eur J*, 2021, 27: 2305–2309
49 Huang NY, He H, Liu SJ, Zhu HL, Li YJ, Xu J, Huang JR, Wang X, Liao PQ, Chen XM. *J Am Chem Soc*, 2021, 143: 17424–17430
50 White JL, Baruch MF, Pander Iii JE, Hu Y, Fortmeyer IC, Park JE, Zhang T, Liao K, Gu J, Yan Y, Shaw TW, Abelev E, Bocarsly AB. *Chem Rev*, 2015, 115: 12888–12935